Permanent Magnet Assisted Synchronous Reluctance Machine Design for Light Traction Applications

Mauro Di Nardo, *Member, IEEE*, Gianvito Gallicchio, *Member, IEEE*, Francesco Cupertino, *Senior Member, IEEE*, Oğuz Korman, Meiqi Wang, Chris Gerada, *Senior Member, IEEE*, Vasyl Varvolik, *Graduate Student Member, IEEE*, Shuo Wang, *Member, IEEE*, Giampaolo Buticchi, *Senior Member, IEEE*.

***Abstract*—This paper presents a systematic comparative design study of permanent magnet assisted synchronous reluctance (PMaSyR) machines for a light traction application aimed at considering an holistic approach for a given outer envelope and cooling system specification. Electromagnetic, structural and thermal aspects are all accurately considered in a computationally efficient manner using a hybrid analytical-finite element (FE) design approach. The SyR machine geometries providing the maximum torque with increasing number of poles are identified and their performance deeply investigated with full FE analysis. The study has been carried out considering several requirements in terms of base and maximum speeds with the aim of drawing general design considerations. Results reveal that the optimal pole number from a torque perspective depends on the considered maximum speed. The reasons behind this behavior are fully investigated as well as how and why the optimal geometries change. The optimal SyR machines are then compared also considering the insertion of permanent magnets within the rotor slots with the aim of maximizing the constant power speed range. The rationales behind the selection of the machine to manufacture are then outlined including aspects related to efficiency and demagnetization under the worst short circuit condition in the entire torque-speed range. The optimized machine (after a FE-based design refinement) has been manufactured and tested on an instrumented test bench validating the proposed design approach and the deduced design insights.**

***Index Terms*—Electric vehicle, finite element analysis, high speed, iron losses, iron ribs, permanent magnet, pole pair selection, rotor design, synchronous reluctance machine, traction.**

I. Introduction

THE ever increasing electrification of transportation systems, due to more sustainable and environmental policies, brings the necessity of more efficient and power dense electric powertrains [1]. Indeed, a significant boost of the drivetrains performance of pure/hybrid electric vehicles is required if the latter need to achieve comparable if not superior performance with the traditional internal combustion engine (ICE) vehicle. As a result, the electric machines, one of the essential parts of the powertrain along with the power electronics, must fulfil very challenging requirements [2].

Induction motor (IM), permanent magnet synchronous motor (PMSM), wound field synchronous machine and synchronous reluctance one (SyR) aided by permanent magnet (PMaSyR) are the most commonly adopted electrical machine topologies in transportation systems [3]–[5]. IMs represent the most robust solution in regards with many aspects, i.e. standardized design methodology and manufacturing techniques, good overload capability and wide constant power speed range [6]–[8]. However, they suffers from the inevitable high rotor losses which makes challenging the machine thermal management often requiring an intensive rotor cooling system [9]. PMSMs present advantages in terms of torque density, efficiency and power factor, especially when adopting rare-earth based PMs. However, the unstable supply chain of the rare-earth based PMs leads to high prices volatility [10] and the increasing concerns about the environmental effects associated with the mining process of the rare-earth materials [11]–[13] are the main current issues of this machine topology. Wound field synchronous machines, often in conjunction with a rotary transformer and a rotor-mounted diode rectifier for the field winding supply, are lately gaining renewed interest also in traction application [14]. Indeed, they are rare-earth free and the possibility to control the field winding current leads to an ideally infinite constant power speed range, and an improved efficiency in the medium-high speeds operating points at the cost of a lower efficiency in the low-speed/high-torque region [15]. Alternatively, SyR machines, as their PM counterparts, benefit from lower rotor losses making easier the thermal management. Low power factor and low torque density and restricted constant power speed range are all SyR disadvantages that can be overcome by the permanent magnet assistance [16]. Indeed, such machine topology (PMaSyR) is becoming one of the most used one in the automotive sector [1] given the advantages over the IM in terms of rotor losses and over the pure PMSM in terms of rare-earth material content although its overload capability is limited. All these machine topology shows a different behaviour in terms of efficiency in the torque-speed plane [3], [17]; as a consequence, the machine topology selection is strictly

M. Di Nardo, G. Gallicchio and F. Cupertino are with the Department of Electrical Engineering and Information Technology, Politecnico di Bari, Bari, 70126 Italy (e-mail: mauro.dinardo@poliba.it, gianvito.gallicchio@poliba.it, francesco.cupertino@poliba.it)

O. Korman, M. Wang and C. Gerada are with the Power Electronics, Machines and Control Group, University of Nottingham, Nottingham, NG7 2RD, UK. (e-mail: oguz.korman@nottingham.ac.uk, meiqi.wang1@nottingham.ac.uk, chris.gerada@nottingham.ac.uk)

Vasyl Varvolik, Shuo Wang and Giampaolo Buticchi are with the Zhejiang Key Laboratory for More Electric Aircraft Technologies, University of Nottingham Ningbo China. Ningbo, 315100 China. (e-mail: vasyl.varvolik@nottingham.edu.cn, shuo.wang@nottingham.edu.cn, buticchi@ieee.org)

dependent on the specific application requirements, i.e. rated specifications, driving cycle, overload capability and behaviour under fault condition, e.g. active short circuit or uncontrolled generator operation. Many studies have been published in the last decades focusing on specific design aspects, such as minimizing the peculiar machine bottleneck, e.g. torque ripple for SyR machine [18], demagnetization in short circuit condition for PM-based machine [19], rotor loss management for the IM [9]. More general design study target the improvement of the power density and the efficiency over the driving cycle while respecting the torque specifications and keeping into consideration the cooling system capability and the rotor structural integrity [6], [20], [21]. In the last few years, a conspicuous amount of literature has also focused on the winding technology with particular emphasis on the hairpin winding which guarantees an improved performance repeatability and reliability of the final product when compared to the more common random wound distributed winding [22]. Many of the aforementioned studies focus on the design optimization of specific case study which considers a given set of preliminary choices which typically include the machine topology and the number of poles [23], [24]. The latter enormously affects several aspects of the powertrain performance. Indeed, the number of poles obviously influence the maximum torque for a given outer envelope but also affect the iron losses along with the AC copper losses at high speed. In addition, when considering a PMaSyR machine which has a complicated rotor geometry, the number of poles also affect the structural behaviour and so the mechanical design.

This works tries to fill this gap presenting a comparative design study of several PMaSyR machines systematically considering all the trade-offs involved when designing such machine topology for a given outer envelope and cooling system specification, i.e. keeping constant the total machine losses. This paper extends the hybrid analytical-FEA design approach outlined in [24]–[30] by considering the number of poles and maximum speeds within the design workflow. The adopted design approach is able to fully consider the effects of the magnetic saturation, the structural strengthening rotor iron ribs and the iron losses on torque, power factor and optimal geometries. The presented study is carried out considering the requirements of a lightweight traction application in terms of base and maximum speeds as well as key electromagnetic specifications. The design methodology is outlined in section II, while section III reports a wide range of designs of SyR machines with different number of poles and maximum speeds sharing the same cooling system and outer envelope as reported in [30]. In section IV, the optimal SyR machines are analyzed in detail identifying the roots of cause of the obtained performance trends. The PM insertion methodology is reported in section V with the considerations on how the PM torque contribution change with the number of poles. Section VI outlines the rationals behind the selection of the optimal number of pole pair including efficiency and demagnetization in the full torque-speed range. The design optimization refinement is described in section VII while the experimental assessment of the prototype of the optimal design is shown in section VIII. The adopted design methodology is summarized in the flowchart shown in Fig. 1.

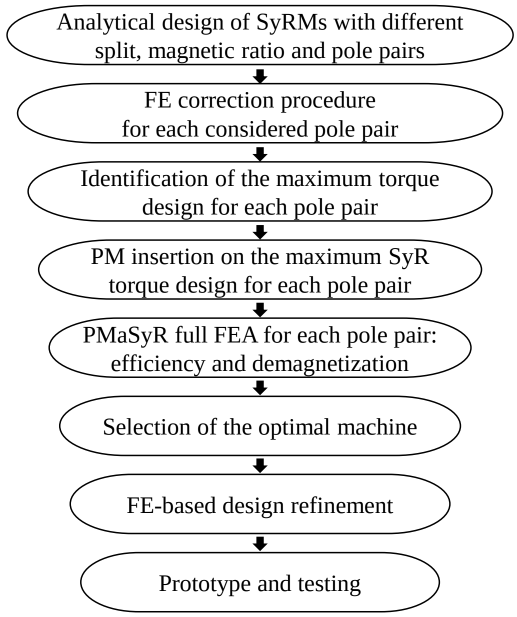

Fig. 1: Flowchart of the proposed approach.

II. Design approach overview

Torque (T) and the internal power factor (ipf) of synchronous reluctance machines can be always expressed as function of inductances and stator currents. Their expressions can be written in the d-q reference frame as:

$$T = \frac{3}{2} \cdot p \cdot (L_{dd} - L_{qq}) \cdot i_d \cdot i_q + \frac{3}{2} \cdot p \cdot L_{dq} \cdot (i_q^2 - i_d^2) \quad (1)$$

$$ipf = \sin\left[\arctan\left(\frac{i_q}{i_d}\right) - \arctan\left(\frac{\lambda_q}{\lambda_d}\right)\right] \quad (2)$$

where p is the number of pole pairs, i_d and i_q are the d- and q-axis currents, λ_d and λ_q are the d- and q-axis fluxes, L_{dd} and L_{qq} are the d and q-axis self-inductances and L_{dq} is the cross-coupling one. The torque equation has been written so to highlight two different terms: the first one is the torque without considering the cross-coupling effects, whereas the latter accounts for the cross-saturation phenomenon. The self inductances L_{dd} and L_{qq} can be seen as the sum between a magnetizing components (L_{dm} and L_{qm}) and a leakage one (L_{ds} and L_{qs}) which in turn can be expressed as follows:

$$L_{ds} = L_{slot} + L_{ts} \quad (3)$$

$$L_{qs} = L_{slot} + L_{ts} + L_{rib} \quad (4)$$

where L_{slot} and L_{ts} account for the flux leakage in the stator slots and tooth shoe respectively; differently, the flux short-circuited via the iron ribs is modelled by the inductance L_{rib} which can be computed either via a simplified analytical formulation as in [25], [26] or by solving the q-axis magnetic circuit as in [31]. The accuracy of the above calculations is crucial for the correct estimation of the two main machine performance indicators, namely T and ipf. Both the inductances and the d- and q-axis currents are clearly function of the machine geometry which can be defined considering a certain number of design choices and assumptions. In the following, the adopted design methodology is briefly re-called.

A. Stator and rotor design

The design exercise starts with the definition of two independent design variables, namely split ratio sr and magnetic ratio mr, defined as follows:

$$sr = \frac{r_r}{r_s}, mr = \frac{B_g}{B_{fe}} \tag{5}$$

where r_r and r_s are the rotor and stator outer radii respectively, B_g is the first harmonic of the airgap flux density and B_{fe} is the peak value of the flux density within the stator yoke. For a given outer envelope (i.e. r_s and the active axial length l_{fe} are fixed) and a given magnetic load B_{fe}, the combination $sr - mr$ determines the complete stator and rotor geometries shown in Fig. 2. Indeed, the stator can be described by two parameters, the tooth width w_y and yoke thickness l_y, which can be easely determined as follows:

$$w_t = \frac{2\pi \cdot sr \cdot r_s \cdot mr}{6qp}, l_y = \frac{\pi}{2}\frac{sr \cdot r_s \cdot mr}{p} \tag{6}$$

where q is the number of slots per pole per phase. The tooth length follows by geometrical considerations since the stator outer radius r_s is fixed:

$$l_t = r_s - r_r - g - l_y - l_{ts} \tag{7}$$

where l_{ts} is the tooth shoe height that, together with the slot opening, complete the description of the stator geometry.

The rotor geometry can be also expressed as function of the above defined independent design variables sr and mr. Indeed, the identification of the flux barriers height h_c^i and their surface S^i can be performed by imposing a constant permeance with respect to the rotor layers and the total iron width equal to l_y [32].

Differently, the widths of the structural iron ribs (w_r), necessary to preserve the rotor integrity, are calculated by adopting a simplified formulation which only accounts for the steady-state centrifugal force acting on each flux guide [33]. Although this approach to define the strengthening ribs is approximate, as it only define the size but not the rib distribution per barrier, is effective [34] and computationally inexpensive. The distribution along the barrier of the iron ribs has to be defined in the final FE-based design refinement stage.

B. Current components calculation

The d-axis current can be computed applying the Ampére law, as in (8):

$$i_d = \frac{\pi}{3}\frac{k_c g}{\mu_0}\frac{p}{k_w N_s}B_g \tag{8}$$

where k_c is the Carter's coefficient, g is the airgap thickness, k_w is the winding factor and N_s is the number of turns in series per phase. When a constant stator losses design scenario is considered during the design exercise, as in this case, the q-axis current component is computed knowing the maximum current I_n which is a function of the cooling system capability (k_{cool}):

$$I_n = \frac{1}{3N_s}\sqrt{\frac{k_{fill}A_{slots}}{2\rho_{cu}(l_{fe}+l_{ew})}(2\pi r_s l_{fe} k_{cool} - P_{fe})} \tag{9}$$

where k_{fill} is slot's filling factor, A_{slots} is the slot area, ρ_{cu} is the copper resistivity, l_{fe} and l_{ew} are the active axial length and the end-winding length respectively, while P_{fe} are the stator iron losses, which are frequency dependent according to the Steinmetz equation. It is worth to underline that the above calculation considers both Joule and iron losses, therefore when comparing different geometries, the total stator losses remain the same as the study is carried out for a fixed outer envelope (e.g. r_s, l_{fe}). This allows a fairer comparison between different machines as all designs can share the same cooling system.

C. Inductances computation

When only the d-axis is supplied, the rotor magnetic potentials are zero therefore L_{dm} may be computed simply as in (10):

$$L_{dm} = \frac{\pi}{2}\mu_0 k_w \left(\frac{N_s}{p}\right)^2 \frac{r_s l_{fe}}{k_c g}\frac{sr}{k_{sat}} \tag{10}$$

where k_{sat} is a coefficient which accounts for the saturation of the d-axis magnetic circuit [25]. Differently, a magnetic equivalent circuital approach has to be adopted for the calculation of the q-axis inductance since the latter depends on the permeances of the saturated iron ribs, flux barriers and flux guides. In the q-axis equivalent circuit (Fig. 3a refers to only one barrier) R_b^i and R_g^i are the reluctances of the flux barriers and the airgap respectively, whereas the ribs influence is taken

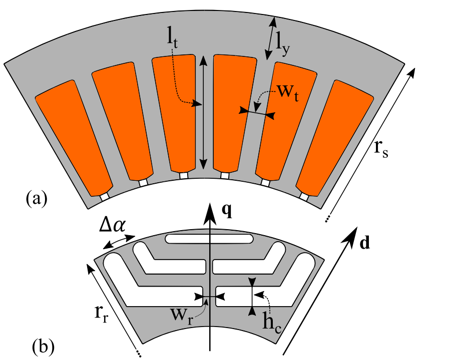

Fig. 2: Stator (a) and rotor (b) parametrization.

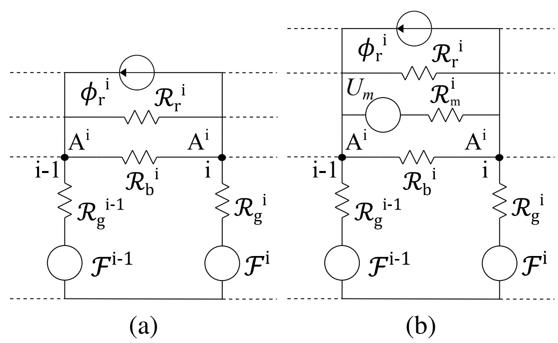

Fig. 3: a) SyR q-axis magnetic circuit, b) PMaSyR q-axis magnetic circuit.

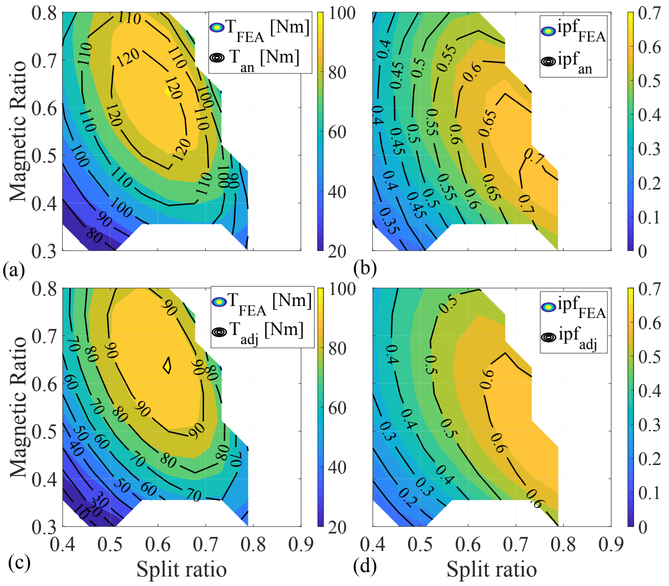

Fig. 4: Torque and internal power factor contours in the design plane calculated with the pure analytical approach (a,b) and the proposed hybrid methodology (c,d) compared to the full FEA.

into account by the parallel between the flux generator ϕ_r^i and R_r^i. The generator F^i accounts for the stator magneto-motive force, while A^i represent the rotor magnetic potentials. The resolution of this circuit, whose detailed description can be found in [31], leads to the calculation of the q-axis inductance.

D. FE-adjustment of the analytical estimations

The described analytical procedure allows obtaining an overall good estimation of both the d-axis and q-axis self inductances, thus leading to a good match between the analytical calculation of the first member of eq. (1) and its FE computation. However, both the neglected cross-couplings effects and the simplified estimation of the iron losses leads to the torque and ipf mismatches shown in Fig. 4a and 4b when compared with a full-FE approach. Such study has been performed considering the parameters outlined in Table I. These drawbacks can be tackled by adopting an adjustment procedure which have been first proposed in [25], [26]. It consists of performing few FE-simulations (i.e. only 4 machines of $sr - mr$ plane) thus obtaining corrections factors for the inductance terms and the iron losses. Then, the extension of such factors to the overall design plane using a linear interpolation allows considering all the disregarded aspects of the analytical model. A detailed description of the proposed approach can be found in [26]. For the sake of clarity 4c and 4d show the comparison between adjusted and FE results, highlighting an excellent agreement.

III. Comparative designs exercise

The above described procedure is suitable to be embedded within a systematic design exercise where SyR machines featuring different pole numbers and base speeds can be examinated considering a lightweight traction application. The assumptions and design choices shown in Table I will be

TABLE I: Unchanging parameters and common assumptions

Parameter	Value	Units
Outer stator radius	123	mm
Stack length	120	mm
Cooling capability	25000	W/m^2
n° of flux barriers per pole	3	-
Maximum stator yoke flux density	1.4	T
Maximum stator tooth flux density	1.8	T
Air gap thickness	0.7	mm
Lamination yield strength (M235-35A)	360	MPa

hereafter considered. Furthermore, a single layer distributed winding featuring a number of slots per pole per phase equal to 2 is adopted and the maximum speed is assumed to be 3.5 times higher than the base speed for all machines. The first speed is used for the sizing of the structural iron ribs, whereas the latter is considered in the calculation of the iron losses at rated condition.

Fig 5 shows the outcome of this analysis in terms of torque and internal power factor contours in the $sr - mr$ plane for different number of poles and design speed. The same figures also report the location of the maximum torque and maximum ipf designs, leading to the following considerations.

- The behavior of T and ipf over the $sr - mr$ plane is different when considering a given pole pairs and speed scenario, thus leading to different locations of the maximum torque and power factor solutions. Indeed, while the ipf depend on both saliency ratio L_d/L_q and current phase angle, the torque is dependent by the number of pole pairs, the difference between the d and q-axis self inductances and the d- and q-axis currents when neglecting the cross-coupling in eq. (1). It follows that by analyzing the different distributions in the design plane of the above quantities, it is possible to infer the reason behind the torque and power factor different shapes in the $sr - mr$ plane when varying poles and speed. In Fig. 6 the trends of the factors affecting the torque and ipf production when considering a design speed of 10.5 kprm and different pole pairs are reported.
- For a given $p - w_{max}$ combination, the location of the maximum ipf designs is always around the region of the $sr - mr$ plane where the saliency ratio is higher (i.e, high sr and low mr) as shown in the contours reported in the first column of Fig. 6. Differently, the location of the maximum torque design is given by the compromise between several aspects which include the needs of maximizing the inductance difference (high sr), the d-axis current (low sr and high mr) and the q-axis one (low sr and mr).
- Furthermore, the trade-off between the above quantities change as the number of poles increases, moving towards higher split ratio and lower magnetic ratio. The reason behind such trend can be inferred by the following considerations: the shape of the $p(L_d - L_q)$ and i_d contours do not change significantly with the poles number while i_q does change (rotating counterclockwise as p increases) thus justifying the change of the maximum torque design location.

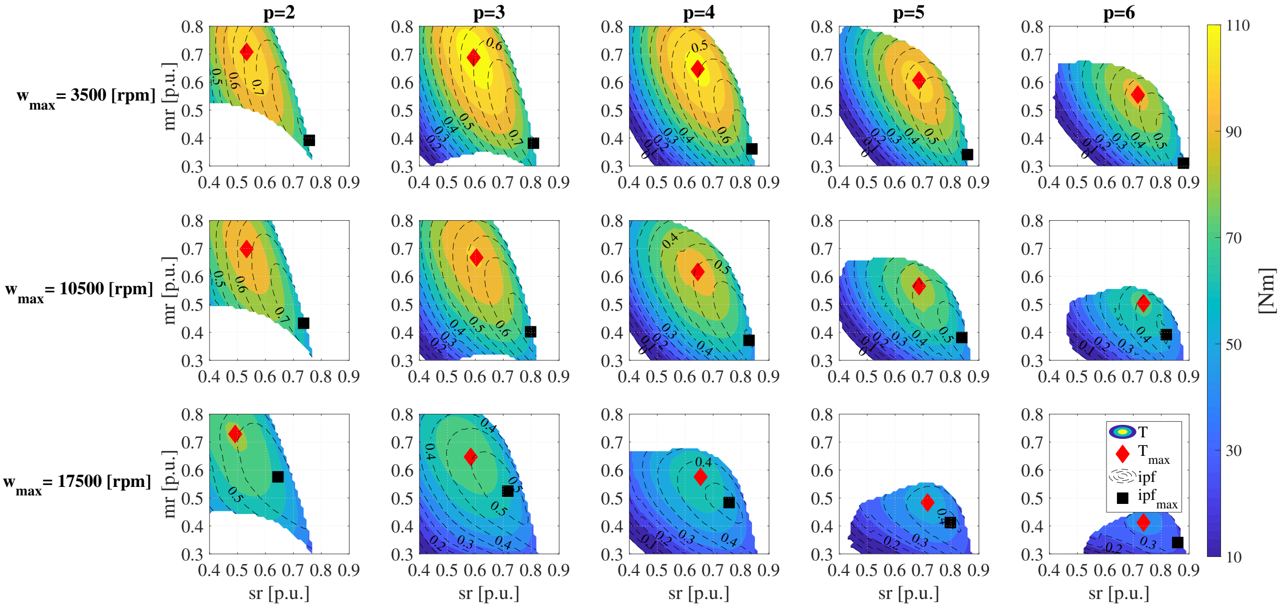

Fig. 5: Torque and internal power factor contour in the $sr - mr$ design plane for $p = 2, 3, 4, 5, 6$ and $w_{max} = 3500, 10500, 17500 rpm$

- Also the cross-coupling has an effect on the location of the maximum torque design. The last column of Fig. 6 shows the percentage of torque due to the cross-coupling (T_{cross}). The torque reduction due to the cross-coupling decreases as mr increases and it moves towards higher sr as the pole pair increases (due to the rotation of i_q contour). Such behavior contributes to move the maximum torque design towards higher magnetic ratio when considering higher number of poles.

The torque contours also change as the maximum speed increases but it depends on the considered number of poles. Indeed, as the speed increase the location of the maximum torque designs moves towards lower sr and higher mr when considering low p; differently, slightly higher split ratio and lower magnetic ratio characterized the maximum torque design as the speed increases when p is higher. Clearly, as also deeply investigated in [26], these behaviors are hugely dependent by the considered soft magnetic material and by the balance between the structural (in terms of iron ribs) and thermal (in terms of iron losses) requirements as the speed increases. In general, the speed increment leads to performance degradations regardless the number of poles. In fact, the rise of both structural iron ribs and iron losses results in a torque and power factor drops. The latter is ascribed to the increment

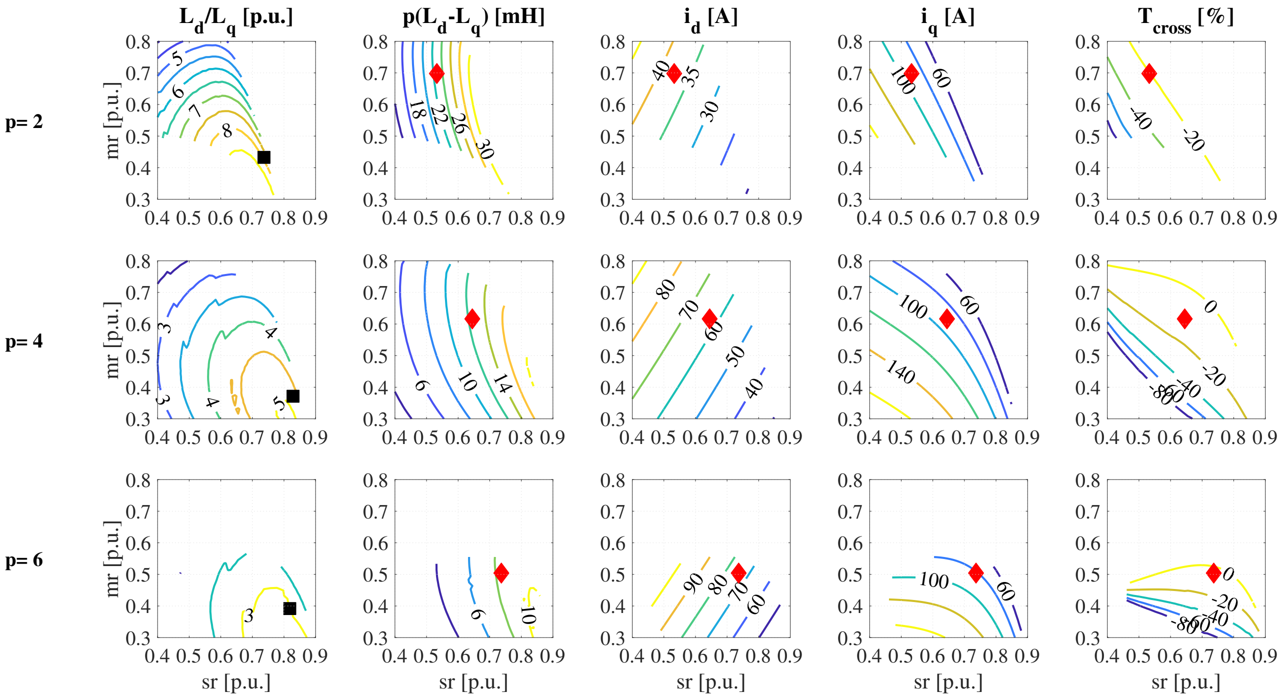

Fig. 6: Saliency ratio, self-inductance differences multiplied by the pole pair, d- and q-axis current, and cross coupling torque contribution contours when considering machines with 4, 8 and 12 poles and a maximum speed of 10.5 krpm.

of the q-axis inductance caused by the wider iron ribs whereas the torque drop is also due to the reduction of the maximum current since a constant stator losses scenario is considered (i.e. reduction of the copper losses quota as the iron losses one increases).

Regardless the speed adopted during the design, the ipf always decreases with the number of poles. The reason behind this trend can be explained considering the reduction of the saliency ratio as p increases as shown in the first column of Fig. 6.

Differently, the design speed influences the torque behavior as the poles number changes:

- for low maximum speed, the torque tends first to increase and then to decrease with the pole numbers;
- for high maximum speed, the torque monotonically decreases with the poles.

The above behaviour will be better explained in the next section where the maximum torque designs will be investigated.

IV. Analysis of the optimal machines

Fig. 7 reports the performance of the maximum torque design in terms of torque and internal power factor. The latter decreases with the speed with a rate of almost 30% regardless the number of pole pairs, whereas the rate of the torque decrement is dependent by the number of poles. Indeed, higher p implies higher iron losses which in turn determines a faster decrement of the torque due to the reduction of the q-axis current. It is worth noticing that the optimal poles number (i.e. the poles number maximizing the torque) depends on the design speed; indeed:

- for low speed designs, the optimal pole number is 6;
- the high speed designs, the optimal pole number is 4;

The rationale behind this behavior can be inferred by analyzing the trends of the factors which mainly affect the torque production. The latter are reports in the left column of Fig 8 when considering a given combination of $sr - mr$ and two different speeds. The torque is the compromise between the descending trend of $\frac{3}{2}p(L_{md} - L_{mq})i_d$ and the ascending/descending trend of the q-axis current. The first trend is due to the fact the L_{mq} decreases less than $1/p^2$, whereas the latter one can be explained by considering the trade-off between the increasing available slot area with p and the rising the iron losses. On one hand, when a higher speed scenario is considered, the higher iron losses leads to

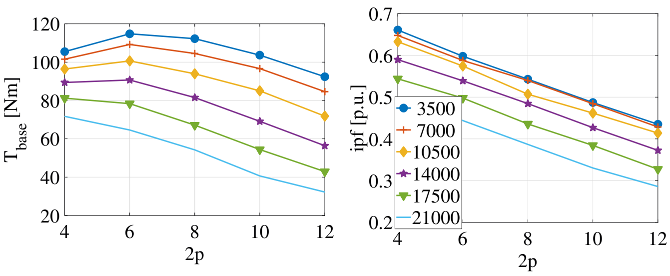

Fig. 7: Torque and internal power factor of the maximum torque design as function of both pole number and base speed.

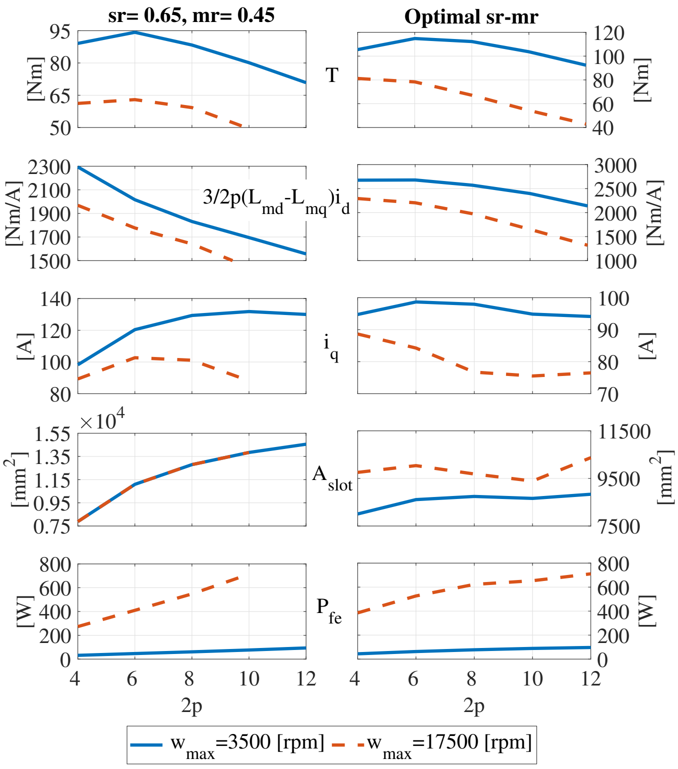

Fig. 8: Torque T, $3/2p(L_{md} - L_{mq})i_d$ factor, q-axis current i_q, slot area A_{slot} and iron losses P_{fe} as function of the pole pair p for a given couple of $sr - mr$ and for the machine providing the maximum torque for two different maximum speeds.

a shift of the maximum i_q toward lower p, since the lower the number of poles the lower the iron losses. On the other hand, the iron losses affect less the lower speed designs therefore p can be increases up to 10 without worsening the i_q current; above 10 poles, the geometrical constraints of the slot area (which can not be increased indefinitely) leads to a plateau of the q-axis current. The same variables are shown in the right column of Fig. 8 while considering the $sr - mr$ combination providing the maximum torque, confirming the aforementioned behaviour although the machine geometry main parameters ($sr - mr$) change with the pole number and speed.

V. Addition of permanent magnets

The above analysis have been performed at the rated conditions considering a pure SyR machine without any permanent magnets within the rotor flux barriers.

The addition of the PMs allows to improve torque, power factor and constant power speed range. As a consequence, a design criteria needs to be chosen in order to size the PMs and maximize a certain performance index. In the following, the natural compensation [31] approach will be applied so to maximize the constant power speed range. In particular, this condition is achieved when the flux produced by the PMs (λ_{PM}) equals the q-axis current one at the rated condition:

$$\lambda_{PM} = L_q I_n \tag{11}$$

This PM design criterion may be elegantly implemented by making the fluxes entering the branches of the stator m.m.f generators (shown in Fig. 3b with the symbol F^i) equal to zero. The iterative resolution of the magnetic circuit to impose the natural compensation criterion can be found in [31] and it is not here reported for the sake of brevity.

This method has been applied to design the PMs to be inserted within the rotor slots of the SyR optimal torque solutions designed for a maximum speed of 10.5krpm. These PMaSyR machines have been analyzed using FE simulations to accurately compute the flux and losses maps in the d-q plane. Fig. 9 reports the torque and power as function of the speed of the optimal machines considering the different number of poles with and without the PMs. Clearly, the natural compensation approach to design the PM quantities allows to achieve the desired constant power speed range and reaches the power at base and max speed of 40kW. Analysing Fig. 9, it can be noticed that the machine having 6, 8 and 10 poles provide very similar results in terms of rated power-speed curve. In the next section, a more in-depth analysis looking at the efficiency and the worst PM demagnetization in the entire torque-speed plane will be reported with the aim of identifying the final machine to be FE-refined and then manufactured and tested.

The torque (T_{tot}) of the obtained PMaSyR machines can be obviously seen as the sum of two contributions, i.e. the reluctance T_{rel} and the PMs T_{PM} ones where:

$$T_{rel} = \frac{3}{2}p(\lambda_{d-rel} \cdot i_q - \lambda_{q-rel} \cdot i_d) \tag{12}$$

and

$$T_{PM} = \frac{3}{2}p(\lambda_{d-PM} \cdot i_q - \lambda_{q-PM} \cdot i_d) \tag{13}$$

Fig. 10 reports the trends of the variables affecting the rated reluctance and PM torque components for the optimal PMaSyR machines with different pole pairs. In particular, Fig. 10a shows that the reluctance torque remains almost constant going from 4 to 6 poles and then decreases reaching the minimum at 12 poles. The same subplot reports an opposite

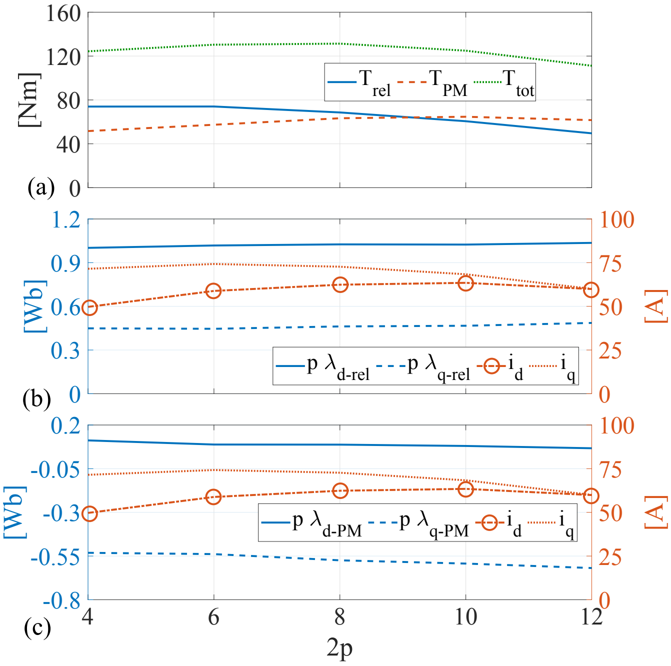

Fig. 10: a) Torque components at rated condition of the obtained PMaSyR hing different pole pairs, b) factors affecting the reluctance torque c) and the PM torque.

trend of the PM torque which increases up to 10 poles and then remain almost constant. As a consequence, the machines having 6 and 8 poles shows a slightly higher overall torque respect to lower or higher pole pairs. As described in Section V, the reluctance torque trend can be mainly ascribed to the behaviour of the current components as function of p as both factors $p\lambda_{d-rel}$ and $p\lambda_{q-rel}$ remains constant with the poles as evident in Fig. 10b. The same can be stated also for the PM torque contribution as both factors $p\lambda_{d-PM}$ and $p\lambda_{q-PM}$ do not change significantly as per Fig. 10c (the former being due to the cross-coupling). The component i_q slightly increases up

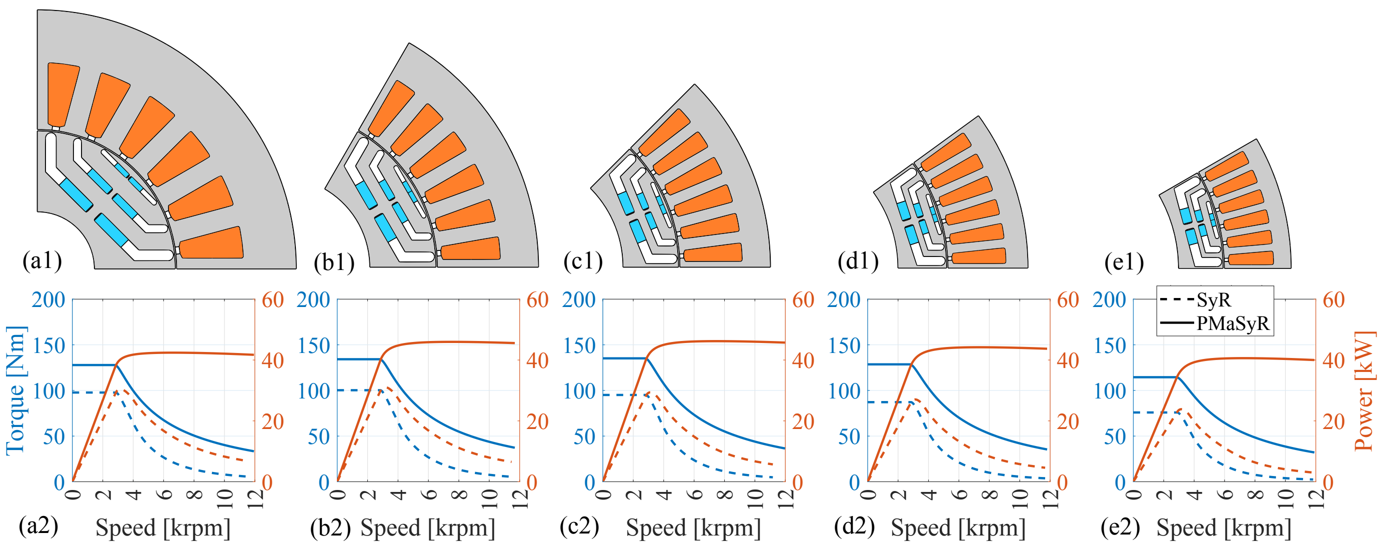

Fig. 9: Cross section and torque and power speed curves of SyR and PMaSyR machines (max speed 10500 rpm) when considering the 2 (a), 3 (b), 4 (c), 5 (d) and 6 (e) pole pairs scenarios.

to 6 poles and then decreases due to the increasing influence of the iron losses as explained analysing Fig. 8 in the previous section. Differently, the magnetizing component i_d increases with the poles (see eq. 8). Consequentially the reluctance torque tends to decreases with p due to both reduction of the term $\lambda_{d-rel} \cdot i_q$ and increment of the term $\lambda_{q-rel} \cdot i_d$. On the contrary, the PM torque tends to increase with p mainly due to the ascending trend of i_d.

VI. Selection of the final design

In terms of rated power-speed envelope, all the obtained PMaSyR designs feature very similar performance, with the best being the 6, 8 and 10 poles as the extreme ones shows a slightly lower power at maximum speed. With the aim of selecting the machine to be refined and manufactured the efficiency in the entire torque-speed range and the worst PM demagnetization have been analyzed.

The first row of Fig. 11 reports the efficiency contour in the torque-speed plane for all the PMaSyR machines along with the torque profiles at half-load, rated load and overload (twice the rated current). It is clear that the efficiency decreases with the number of pole pairs; this is an expected result since higher poles implies higher fundamental frequency and so higher iron losses.

The PM demagnetization can occur when the q-axis flux against the permanent magnets is significant ($L_q \cdot i_q$). The demagnetization check is usually performed considering a q-axis current component equal to two or three times the rated one. However, a worse condition can occur when the machine is subject to a three-phase short circuit. The behaviour of the d- and q-axis currents during the short circuit depends on the pre-fault conditions, i.e. current components (torque) and speed. The calculation of the short-circuit current as a function of the pre-fault operating point can be performed either adopting a transient FEA or solving the differential equations governing the short circuit using the flux-current maps identified via static FEA as suggested in [35]. The latter approach has been adopted since it allows to accurately compute the short-circuit current with a negligible computational time if compared to a full transient FEA. Fig. 12 shows the i_d and i_q short-circuit currents as function of the time for the 4-poles machine when the pre-fault condition is the overload one at base speed. The figure also highlights the maximum positive i_q current which is the worst value to be considered for the PM demagnetization analysis.

The second row of the Fig. 11 reports the maximum positive q-axis current during the short-circuit in the torque-speed plane, i.e. as a function of the pre-fault condition. Regardless the number of pole pairs, the maximum peak short circuit q-axis current always occur when the pre-fault condition is the overload at base speed as also inferred in [35].

With the aim of investigating the state of the PMs, each PMaSyR has been FE-evaluated imposing the just calculated worst case short circuit currents. The results of such analysis are shown in the third row of Fig. 11. The latter shows the demagnetization proximity DM_{prox} defined as:

$$DM_{prox} = B_{rot} - B_{kneePM} \tag{14}$$

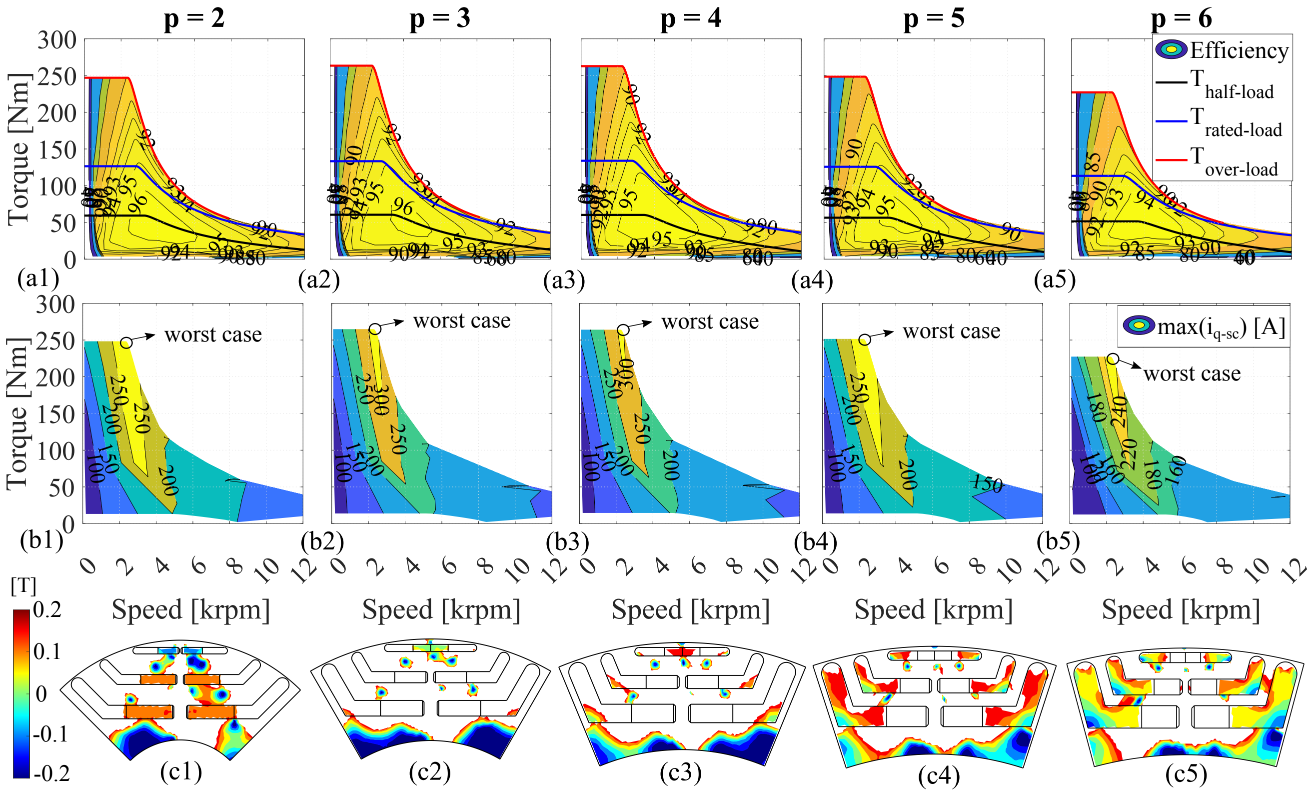

Fig. 11: (a) Efficiency and (b) maximum q-axis short-circuit current over the torque-speed plane for different pole pairs and (c) demagnetization proximity map in the worst short circuit scenario.

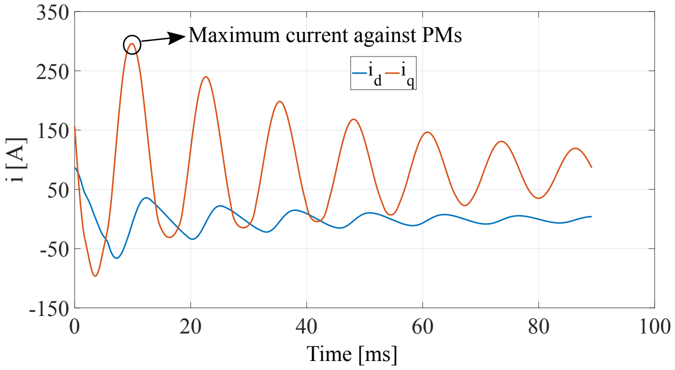

Fig. 12: Dynamic behavior of d-axis and q-axis current during short circuit of the 4-poles PMaSyR machine when the pre-fault condition is overload at base speed.

i.e. the difference between the flux density at a given point in the rotor (B_{rot}) and the knee value of the PM material (B_{kneePM}). Analysing these maps, which shows only rotor regions where $B < 1[T]$, it is clear that only the 4-poles machine presents a visible demagnetization of the outermost PMs. No demagnetization issues are experienced by the other cases and the minimum of the PM flux density B_{PM} increases with the poles. It can be stated that the higher the number of poles, the lower is the demagnetization risk.

The rationale behind this behavior can be inferred by analysing Fig. 13 which reports the behaviour with the poles of the variables affecting the PM demagnetization, i.e. the q-axis current, flux and inductance.
The first subplot (Fig. 13a) shows that the pre-fault PM flux

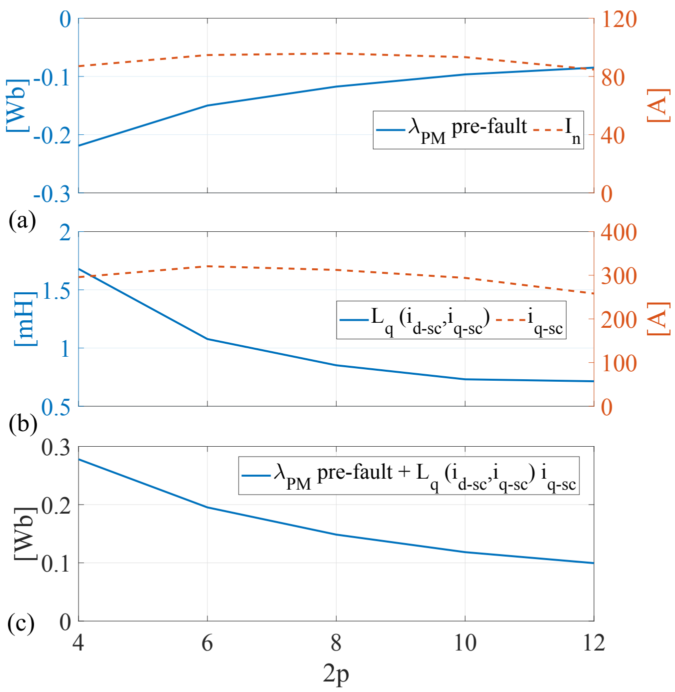

Fig. 13: (a) pre-fault PM flux and the rated current, (b) the maximum q-axis short circuit current and q-axis inductance at the maximum short-circuit current and (c) sum between the pre-fault PM flux and the q-axis short-circuit flux as function of the pole pairs.

(index of the "strength" of the PM before the short-circuit) decreases with the number of pole pairs. This is due to the fact that the PMs have been designed with the natural compensation criterion, i.e. imposing the PM flux linkage equal to the product between q-axis inductance and rated current. The latter (I_n) does not change significantly with the number of poles (as shown in Fig. 13a) while the q-axis inductance is almost inverse proportional with the square of the poles. As a consequence, the absolute value of the PM flux decreases with the poles (because L_q decreases).
The maximum short-circuit current against the PMs (i_{q-sc}) is barely influenced by the pole number, whereas the q-axis inductance in the worst short-circuit condition ($L_q(i_{d-sc}, i_{q-sc})$) decreases with p (Fig. 13b).
It follows that the sum between the pre-fault PM flux and the q-axis flux due to i_{q-sc} decreases with the poles (Fig. 13c). In other words, since the sign of the pre-fault PM flux is negative, the effect of the short-circuit q-axis flux ($L_q(i_{d-sc}, i_{q-sc}) \cdot i_q$) will be less impactful on the PMs in terms of demagnetization.

According to the above considerations regarding rated performance, efficiency and worst demagnetization scenario, the 6 poles design has been selected as the solution to be further refined. Indeed, it shows the same rated performance of the 8 poles machine but with a higher overall efficiency and no demagnetization issues when compared to the 4 poles one.

VII. Design Optimization Refinement

The design procedure outlined in the previous sections allowed to drastically narrow down the range of the possible solutions to analyse in detail with a more accurate performance evaluation method. Indeed, the initial design shown in Fig. 9b1 requires to be refined as both torque ripple and structural performance have not been accurately considered during the analytical design stage. For these reasons, in the following subsections, the design optimization refinement study is described first outlining the geometrical variables to identify and then showing the results of the optimization. It is worth to underline that the design refinement has been implemented as a local search around the analytically optimal solution.

A. Parametrization of the PMaSyR Machine

The stator geometry, previously shown in Fig. 2, is parametrized in per unit, all shown through (15) to (17), where k_{l_t} is the ratio between slot depth and total stator thickness, k_{w_t} is the ratio between the tooth thickness and tooth pitch and k_{SO} is the ratio between the slot opening (SO) to maximum available SO (dependent on k_{w_t}).

$$l_t = (r_s - r_r) \cdot k_{l_t} \tag{15}$$

$$w_t = 2 \cdot r_r \cdot \sin(\frac{180}{N_s} \cdot k_{w_t}) \tag{16}$$

$$SO = 2 \cdot k_{SO} \cdot (1 - k_{w_t}) \frac{2\pi r_r}{N_s} \tag{17}$$

The flux barrier profile described by the Joukowski's flow equations [36] are used with rectangular magnets in the middle. The adoption of the above barriers shape allows to

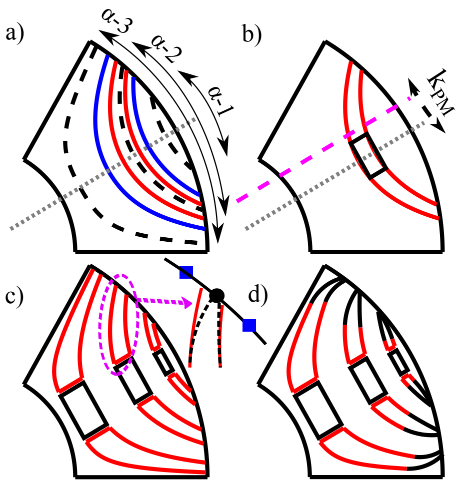

Fig. 14: Parametrization steps of the PMaSyR rotor

increase the machine performance with respect to the easier to analytically model straight barrier geometry [37].

After the flux barrier angles a are defined (which determine the central line of each barrier, see dashed black line in Fig. 14a), the maximum thickness of each barrier can be calculated considering a minimum iron thicknesses between barrier-barrier, barrier-shaft and barrier-rotor surface. Once the maximum barrier thickness is found (on the q-axis), the thicknesses of each barrier can be expressed in per unit (k_t). Actual and maximum barrier thicknesses are shown with red and blue continuous lines respectively in Fig.14 a). Once the thickness of a flux barrier is known, dimensions of the PM for each barrier can be calculated. Thickness (defined on the q-axis) and length of the PM are determined by a single parameter k_{PM}. This parameter primarily determines the length of the PM as a ratio to the length of upper flux line forming a flux barrier. k_{PM} is visualized in Fig.14 b). When k_{PM} is known, thickness of the PM can be found by placing the rectangular shaped PM on the flux lines shown in red. By doing so, the PM thickness is controlled by the thickness of flux barrier and k_{PM}. The resulting geometry is given in Fig. 14c). Adding some additional degrees of freedom, the end point of the barriers might be given a bigger range of variation which in turn can help enhancing the torque ripple characteristics [38]. This modification consists in defining an additional range of variation of end point angle for each barrier. A point (black dot) is selected in the new range (blue dots) with a variable (k_d) in [-1 1]. Once the variable is selected and the end point is known, two arc segments are drawn from the barrier lines and barrier shape drawing is concluded.

B. Optimization

The above described machine parametrization requires a total of 12 variables to be considered during the optimization. These variables and their ranges of variations are given in Table II. Ranges of the variables are selected to vary around the respective variables of the initially selected machine. In order to ensure the mechanical safety, tangential and radial rib thicknesses from the initial design are kept the same. Optimization objectives are selected as maximization of average torque and minimization of torque ripple. During the optimization, one sixth of the electrical period is analyzed with steps of one degree mechanical and with a constant current phase angle of 55^o.

TABLE II: Optimization variables

Name	Range	Number of variables
sr	[0.5 0.7]	1
k_{l_t}	[0.4 0.7]	1
k_{w_t}	[0.4 0.7]	1
k_{PM}	[0.5 0.9]	3
k_a	[0.3 0.5][0.1 0.4][0.1 0.4]	3
k_d	[-1 1]	3

The optimization results are shown in Fig.15. The final design is selected to be in the lower-right corner of the Pareto front having around 127Nm average torque and below 10% torque ripple. The location of the design and the design itself is shown in Fig.15. Compared to the initially selected design, optimization yielded designs having better torque ripple, as shown in Fig. 16 which reports the torque, power and torque ripple curves as function of the speed of both initial and optimized designs considering the same current. It is worth underling that, despite the performance in terms of average torque remain almost identical, the torque ripple is greatly reduced by the application of the optimization procedure. Prior the manufacturing of the selected design, the rotor structural integrity has been verified with a structural FE analysis which has required a minor modifications of the fillet radius of the various corners present in the rotor geometry. Such geometrical modifications does not led to major performance deterioration.

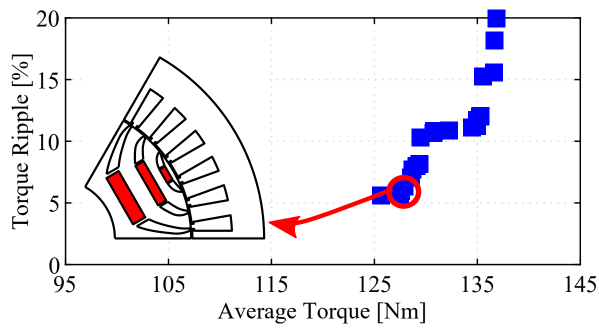

Fig. 15: Optimization results

VIII. Experimental assessment

A prototype of the final design is built for experimental validation. The rotor of the prototype is shown in Fig.17a) after the magnets have been inserted. The control platform with inverter and the test rig are shown in Fig.17b) and Fig.17c). The machine prototype is connected to the cooling system providing a flowrate of 10 litre/minute. A prime mover is used to drive the PMaSyR under test, while the torque measurements are accomplished by a torque meter Kistler

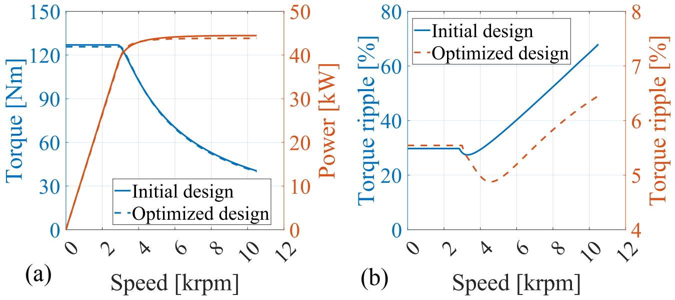

Fig. 16: Comparison between initial and optimized designs in terms of torque/power (a) and torque ripple (b).

4550A coupled between them. The control algorithm is implemented using a dSPACE MicroLabBox platform (DS1202) which controls an IGBT-based 2-level inverter via an interface board with a sampling frequency of 10 kHz and a dead-time of 4μs. The traction application requires working in a wide range of operating points; therefore, experiments aim to reveal the electromagnetic characteristics of the machine in the whole (*d-q*) current plane. The constant-speed magnetic model identification method is implemented [39] to obtain flux linkage and torque characteristics. Flux linkages are estimated using (*d-q*) voltage terms at steady-state, while the spatial harmonics and inverter dead-time effects are eliminated by averaging the measurements over one mechanical period. The resistance voltage drops and inverter non-linearities are taken into account by the average between motoring and generating modes. The reference speed of the prime mover was set to 500 rpm in order to minimize the influence of iron loss while providing a good signal-to-noise ratio of the reference voltages. For each current set-point in the plane, reference currents are fed to the machine, and measurements are taken only after the transient behavior is diminished as highlighted

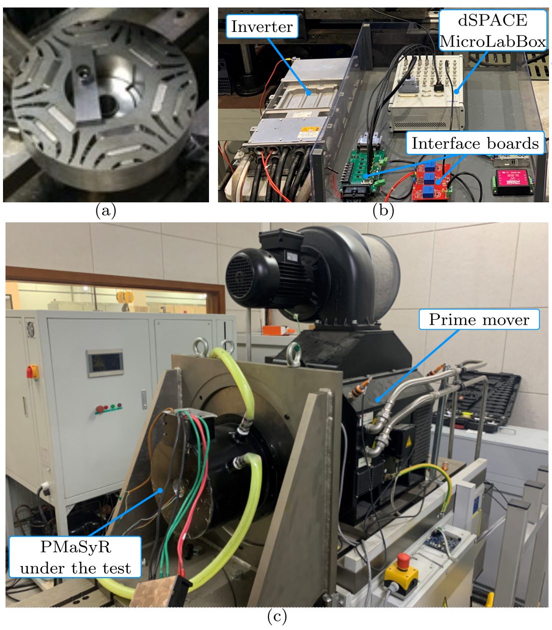

Fig. 17: Prototype motor: (a) rotor, (b) inverter and control platform, (c) test rig.

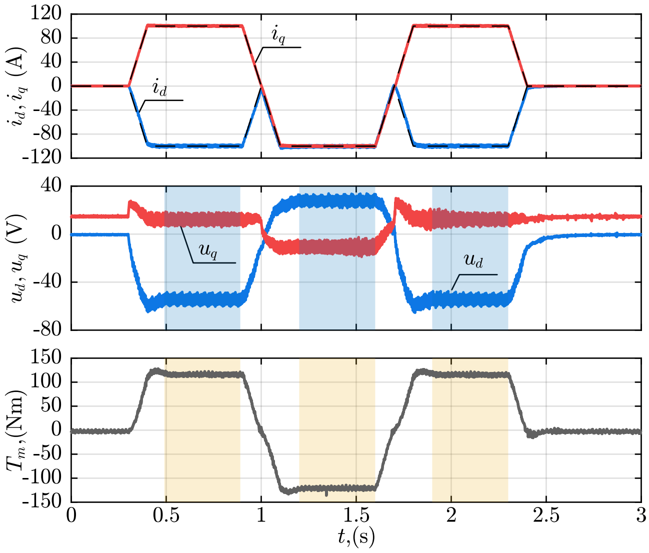

Fig. 18: Identification sequence for one current setpoint.

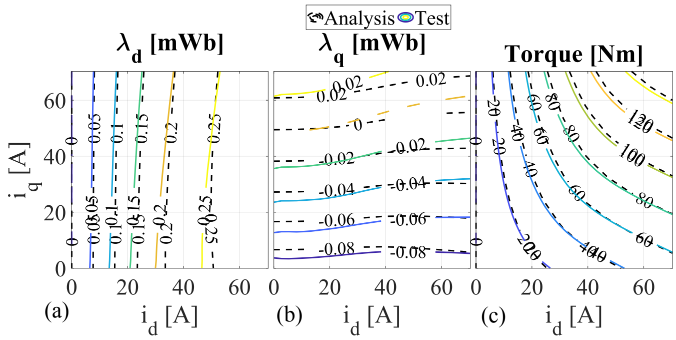

Fig. 19: Comparison between FE and experimental d (a) and q (b) axis flux maps and average torque (c).

in Fig. 18. The latter reports the trends of d-q currents, voltage and torque during the identification of one operating point.

The results of the whole identification procedure are presented in Fig.19 as torque and flux linkages maps in the d-q current plane. The same figures also show the FE-calculated performance; it is clear that there are negligible differences between the measured and expected torque and flux linkages maps.

IX. Conclusion

This paper has presented an holistic design study of PMaSyR machines targeting the requirements of a light traction application. A hybrid analytical-FE design approach has first been outlined able of considering all the trade-offs involved when designing such machine topology for a given outer envelope and cooling system capability. Particular emphasis has been placed on the influence on the number of poles which affects electromagnetic, structural and thermal performance. The study has been carried out considering several requirements in terms of base and maximum speeds with the aim of drawing general design considerations. The main results of the design study can be summarized as follows.

- With increasing speed, torque and power factor decreases for all machines regardless of pole number due to iron losses and structural rib thickness increments.
- The optimal pole pairs from a torque perspective depends on the considered speed. Indeed, it is defined by the trade-off between the conflicting consequences of the rise of the iron losses, available slot area and decreasing anisotropy (as p increases). Low speed applications might benefit from the selection of high pole numbers (6 or 8) while for high speed applications, low number of pole pairs are preferred. Such conclusion is obviously dependent on the considered soft magnetic material which affect the aforementioned compromise.
- As the pole pair increase, the design providing the maximum torque features higher split ratio and lower magnetic ratio since in this direction the q-axis current moves its maximum.
- The addition of the PMs on the optimal (torque wise) SyR designs allows to widen the constant power speed range and make almost identical the rated torque-speed envelope of the machines having different pole pairs.
- The selection of the final machine is the result of the trade-off between efficiency and PM demagnetization. It has been shown that the 4-poles design provide the highest efficiency, but it is the most prone to demagnetize. Differently, machines with higher poles present lower efficiency but no demagnetization issues.

The results of the 6-poles design - the best compromise between all performance indexes - have been experimentally verified through a comprehensive testing campaign, confirming the validity of the proposed technique.

REFERENCES

[1] Iqbal Husain, Burak Ozpineci, Md Sariful Islam, Emre Gurpinar, Gui-Jia Su, Wensong Yu, Shajjad Chowdhury, Lincoln Xue, Dhrubo Rahman, and Raj Sahu. Electric drive technology trends, challenges, and opportunities for future electric vehicles. *Proceedings of the IEEE*, 109(6):1039–1059, 2021.

[2] Chunhua Liu, K. T. Chau, Christopher H. T. Lee, and Zaixin Song. A critical review of advanced electric machines and control strategies for electric vehicles. *Proceedings of the IEEE*, 109(6):1004–1028, 2021.

[3] Lingyun Shao, Ahu Ece Hartavi Karci, Davide Tavernini, Aldo Sorniotti, and Ming Cheng. Design approaches and control strategies for energy-efficient electric machines for electric vehicles—a review. *IEEE Access*, 8:116900–116913, 2020.

[4] Mircea Popescu, James Goss, David Alan Staton, Douglas Hawkins, Yew Chuan Chong, and Aldo Boglietti. Electrical vehicles—practical solutions for power traction motor systems. *IEEE Transactions on Industry Applications*, 54(3):2751–2762, 2018.

[5] Veysel T. Buyukdegirmenci, Ali M. Bazzi, and Philip T. Krein. Evaluation of induction and permanent-magnet synchronous machines using drive-cycle energy and loss minimization in traction applications. *IEEE Transactions on Industry Applications*, 50(1):395–403, 2014.

[6] Emad Roshandel, Amin Mahmoudi, Wen L. Soong, and Solmaz Kahourzade. Optimal design of induction motors over driving cycles for electric vehicles. *IEEE Transactions on Vehicular Technology*, pages 1–15, 2023.

[7] Qian Zhang, Huijuan Liu, Zhenyang Zhang, and Tengfei Song. A cast copper rotor induction motor for small commercial ev traction: Electromagnetic design, analysis, and experimental tests. *CES Transactions on Electrical Machines and Systems*, 2(4):417–424, 2018.

[8] Gianmario Pellegrino, Alfredo Vagati, Barbara Boazzo, and Paolo Guglielmi. Comparison of induction and pm synchronous motor drives for ev application including design examples. *IEEE Transactions on Industry Applications*, 48(6):2322–2332, 2012.

[9] Robin Thomas, Hugo Husson, Lauric Garbuio, and Laurent Gerbaud. Comparative study of the Tesla Model S and Audi e-Tron Induction Motors. In *17-th International Conference on Electrical Machines, Drives and Power Systems (ELMA)*, Sofia (on line), Bulgaria, July 2021.

[10] Mukhammed Murataliyev, Michele Degano, Mauro Di Nardo, Nicola Bianchi, and Chris Gerada. Synchronous reluctance machines: A comprehensive review and technology comparison. *Proceedings of the IEEE*, 110(3):382–399, 2022.

[11] S. Langkau and M. Erdmann. Environmental impacts of the future supply of rare earths for magnet applications. *Journal of Industrial Ecology*, 25(4):1034–1050, 2021.

[12] J. Nayar. Not so green technology: the complicated legacy of rare earth mining. Harvard Int. Review, Cambridge, USA, 2021. Accessed: Jul. 01, 2023. [Online]. Available: https://hir.harvard.edu/not-so-green-technology-the-complicated-legacy-of-rare-earth-mining/.

[13] Saleem H. Ali. Social and environmental impact of the rare earth industries. *Resources*, 3(1):123–134, 2014.

[14] Gaia Petrelli, Stefano Nuzzo, Tianjie Zou, Davide Barater, Giovanni Franceschini, and Chris Gerada. Review and future developments of wound field synchronous motors in automotive. In *2023 IEEE International Conference on Electrical Systems for Aircraft, Railway, Ship Propulsion and Road Vehicles & International Transportation Electrification Conference (ESARS-ITEC)*, pages 1–6, 2023.

[15] Nanjun Tang, Dominick Sossong, Nicholas Krause, Xuliang Hou, Marisa J.T. Liben, Daniel C. Ludois, and Ian P. Brown. Implementation of a metamodel-based optimization for the design of a high power density wound field traction motor. *IEEE Transactions on Industry Applications*, pages 1–10, 2023.

[16] Nicola Bianchi, Silverio Bolognani, Enrico Carraro, Mosè Castiello, and Emanuele Fornasiero. Electric vehicle traction based on synchronous reluctance motors. *IEEE Transactions on Industry Applications*, 52(6):4762–4769, 2016.

[17] Giacomo Bacco, Cristian Babetto, Michele Bonfante, Matteo Carbonieri, and Nicola Bianchi. Efficiency maps computation and comparison including thermal limits. In *2019 IEEE Energy Conversion Congress and Exposition (ECCE)*, pages 4846–4852, 2019.

[18] Yongming Xu, Ziyi Xu, Hengpei Cao, and Wenhui Liu. Torque ripple suppression of synchronous reluctance motors for electric vehicles based on rotor improvement design. *IEEE Transactions on Transportation Electrification*, 9(3):4328–4338, 2023.

[19] Thanh Anh Huynh and Min-Fu Hsieh. Irreversible demagnetization analysis for multilayer magnets of permanent magnet-assisted synchronous reluctance machines considering current phase angle. *IEEE Transactions on Magnetics*, 55(7):1–9, 2019.

[20] Alireza Fatemi, Nabeel A. O. Demerdash, Thomas W. Nehl, and Dan M. Ionel. Large-scale design optimization of pm machines over a target operating cycle. *IEEE Transactions on Industry Applications*, 52(5):3772–3782, 2016.

[21] Bryton Praslicka, Cong Ma, and Narges Taran. A computationally efficient high-fidelity multi-physics design optimization of traction motors for drive cycle loss minimization. *IEEE Transactions on Industry Applications*, 59(2):1351–1360, 2023.

[22] Tianjie Zou, David Gerada, Antonino La Rocca, Mohsen Moslemin, Alasdair Cairns, Mengmeng Cui, Anuvav Bardalai, Fengyu Zhang, and Chris Gerada. A comprehensive design guideline of hairpin windings for high power density electric vehicle traction motors. *IEEE Transactions on Transportation Electrification*, 8(3):3578–3593, 2022.

[23] Tianjie Zou, David Gerada, Salvatore La Rocca, Antonino La Rocca, Adam Walker, Gaurang Vakil, Saúl López Arevalo, Zeyuan Xu, Mengmeng Cui, Anuvav Bardalai, Meiqi Wang, R. M. Ram Kumar, Alessandro Marfoli, Krzysztof Paciura, Richard Barden, Emil Ernest, Shaohong Zhu, Naila Qayyum, Alastair McQueen, Fengyu Zhang, and Chris Gerada. Airgap length analysis of a 350 kw pm-assisted syn-rel machine for heavy duty ev traction. *IEEE Transactions on Industry Applications*, 59(2):1557–1570, 2023.

[24] Chao Lu, Simone Ferrari, and Gianmario Pellegrino. Two design procedures for pm synchronous machines for electric powertrains. *IEEE Transactions on Transportation Electrification*, 3(1):98–107, 2017.

[25] S. Ferrari and G. Pellegrino. Feafix: Fea refinement of design equations for synchronous reluctance machines. *IEEE Transactions on Industry Applications*, 56(1):256–266, 2020.

[26] G. Gallicchio, M. Di Nardo, M. Palmieri, A. Marfoli, M. Degano, C. Gerada, and F. Cupertino. High speed synchronous reluctance machines: Modeling, design and limits. *IEEE Transactions on Energy Conversion*, pages 1–1, 2021.

[27] M. Di Nardo, G. Gallicchio, M. Palmieri, A. Marfoli, G. Lo Calzo, M. Degano, C. Gerada, and F. Cupertino. High speed synchronous

reluctance machines: Materials selection and performance boundaries. *IEEE Transactions on Transportation Electrification*, pages 1–1, 2021.

[28] P. Arumugam, J. Dusek, A. Aigbomian, G. Vakil, S. Bozhko, T. Hamiti, C. Gerada, and W. Fernando. Comparative design analysis of permanent magnet rotor topologies for an aircraft starter-generator. In *Intelligent Energy and Power Systems (IEPS), 2014 IEEE International Conference on*, pages 273–278.

[29] Mauro Di Nardo, Gianvito Gallicchio, Marco Palmieri, Alessandro Marfoli, Michele Degano, Chris Gerada, and Francesco Cupertino. High speed permanent magnet assisted synchronous reluctance machines – part ii: Performance boundaries. *IEEE Transactions on Energy Conversion*, 37(4):2567–2577, 2022.

[30] Oğuz Korman, Mauro Di Nardo, Michele Degano, Chris Gerada, Gianvito Gallicchio, and Francesco Cupertino. On the pole pair selection of synchronous reluctance machines for traction applications. In *2022 International Conference on Electrical Machines (ICEM)*, pages 2114–2120, 2022.

[31] G. Gallicchio, M. Di Nardo, M. Palmieri, A. Marfoli, M. Degano, C. Gerada, and F. Cupertino. High speed permanent magnet assisted synchronous reluctance machines - part i: A general design approach. *IEEE Transactions on Energy Conversion*, pages 1–1, 2022.

[32] A. Vagati, G. Franceschini, I. Marongiu, and G. P. Troglia. Design criteria of high performance synchronous reluctance motors. In *Industry Applications Society Annual Meeting, 1992., Conference Record of the 1992 IEEE*, pages 66–73 vol.1, 1992.

[33] M. Barcaro, G. Meneghetti, and N. Bianchi. Structural analysis of the interior pm rotor considering both static and fatigue loading. *Industry Applications, IEEE Transactions on*, 50(1):253–260, 2014.

[34] M. Di Nardo, M. Galea, C. Gerada, M. Palmieri, F. Cupertino, and Salem Mebarki. Comparison of multi-physics optimization methods for high speed synchrnous reluctance machines. In *IECON 2015 - 41st Annual Conference of the IEEE Industrial Electronics Society*, pages 002771–002776, 2015.

[35] Simone Ferrari, Gaetano Dilevrano, Paolo Ragazzo, Paolo Pescetto, and Gianmario Pellegrino. Fast determination of transient short-circuit current of pm synchronous machines via magnetostatic flux maps. *IEEE Transactions on Industry Applications*, 59(4):4000–4009, 2023.

[36] Reza Rajabi Moghaddam. *Synchronous Reluctance Machine (SynRM) in Variable Speed Drives (VSD) Applications*. PhD thesis, KTH, Electrical Machines and Power Electronics, 2011. QC 20110518.

[37] Matteo Gamba, Gianmario Pellegrino, and Francesco Cupertino. Optimal number of rotor parameters for the automatic design of synchronous reluctance machines. In *2014 International Conference on Electrical Machines (ICEM)*, pages 1334–1340, 2014.

[38] M. Di Nardo, M. Degano, M. Galea, C. Gerada, M. Palmieri, F. Cupertino, N. Bianchi, and D. Gerada. End barrier shape optimizations and sensitivity analysis of synchronous reluctance machines. In *Industrial Electronics Society, IECON 2015 - 41st Annual Conference of the IEEE*, pages 002914–002919, Nov 2015.

[39] E. Armando, R. I. Bojoi, P. Guglielmi, G. Pellegrino, and M. Pastorelli. Experimental identification of the magnetic model of synchronous machines. *Industry Applications, IEEE Transactions on*, 49(5):2116–2125, 2013.

Mauro Di Nardo (M'18) received the M.Sc. (Hons.) degree in electrical engineering from the Polytechnic University of Bari, Italy, in 2012, and the Ph.D. degree in electrical machine design from the University of Nottingham, U.K., in 2017. From 2017 to 2019, he was with the AROL spa leading the R&D team focusing on electrical drives design for mechatronics applications. Between 2019 and 2023, he was with the Power Electronics and Machine Control Group of the University of Nottingham as Research Fellow. He is currently an assistant professor in electrical machine and drives at the Polytechnic University of Bari, Italy. He serves as an Associate Editor for the IEEE Open Journal of Industry Applications and IEEE Transaction on Energy Conversion.

Gianvito Gallicchio received the B.Sc. (Hons.), M.Sc. (Hons.) and the Ph.D. degrees in electrical engineering from the Politecnico di Bari, Bari, Italy in 2016, 2018 and 2023 respectively. He is currently a research fellow with the Electrical Machines and Drives Group, Politecnico di Bari. His main research interests include the analysis, modeling and design optimization of permanent magnet and synchronous reluctance machines for both traction and high-speed applications.

Francesco Cupertino (M'08–SM'12) received the Laurea and Ph.D. degrees in electrical engineering from the Politecnico di Bari, Bari, Italy, in 1997 and 2001, respectively. Since 2001, he has been with the Department of Electrical and Information Engineering, Politecnico di Bari, where he is currently a Full Professor of converters, electrical machines, and drives. He is the Scientific Director of several public/private laboratories at Politecnico di Bari that enroll more than 50 researchers. His research interests include the design of synchronous electrical machines, motion control of high performances electrical machines, applications of computational intelligence to control, and sensorless control of ac electric drives. He has authored or coauthored more than 130 scientific papers on these topics. F. Cupertino is currently the rector of Politecnico di Bari.

Oguz Korman received the B.Sc. and M.Sc. in electrical engineering from Istanbul Technical University, Turkey, in 2015 and 2018, and the Ph.D. degree from the University of Nottingham, U.K. in 2024. Between 2017 and 2019, he was as an Electromagnetic Design Engineer in Istanbul, Turkey, involved in many projects focusing on industrial custom applications. He is currently a research fellow within the Power Electronics, Machines and Control Group at the University of Nottingham, and his research interests include modeling and design of high-performance electric motors for industrial and traction applications.

Meiqi Wang received the B.Eng. degree in electrical engineering from the Northeast Electric Power University, Jilin, China, in 2014. Between 2014 and 2017, she was a joint training master Student in electrical engineering with Tsinghua University, Beijing, China, and Northeast Electric Power University. She gained the Ph.D. degree with the Power Electronics, Machines and Control Group, University of Nottingham, U.K in 2023 where she is currently a research fellow. Her research interests include power electronics and advanced control techniques for high-speed synchronous machines for transportation electrification.

Chris Gerada received the Ph.D. degree in numerical modeling of electrical machines from The University of Nottingham, Nottingham, U.K., in 2005. He was a Researcher with The University of Nottingham, working on high-performance electrical drives and on the design and modeling of electromagnetic actuators for aerospace applications. In 2008, he became a Lecturer in electrical machines, in 2011, as an Associate Professor, and in 2013, a Professor at The University of Nottingham. His main research interests include the design and modeling of high-performance electric drives and machines. He has secured major industrial, European and U.K. grants, authored more than 200 papers and was awarded a Royal Academy of Engineering Research Chair to consolidate research in the field.

Vasyl Varvolik received the B.Sc. and M.Sc. degrees in electrical engineering from the National Technical University of Ukraine "Igor Sikorsky Kyiv Polytechnic Institute," Kyiv, Ukraine, in 2016 and 2018, respectively. He secured the Ph.D. degree in electrical and electronics engineering with the University of Nottingham, Ningbo, China in 2023 where is currently a research fellow. His research interests include high-fidelity simulation, parameter identification, torque ripple reduction, high-performance control of synchronous reluctance, and permanent magnet synchronous motor drives.

Shuo Wang received the Ph.D. degree in control science and engineering from Tongji University, Shanghai, China, in 2019. From 2017 to 2018, he became a Visiting Researcher with Power Electronics, Machines and Control Group, University of Nottingham, Nottingham, U.K. He is currently working as a Senior Research Fellow with the University of Nottingham, Ningbo, China. His research interests include high-performance torque control, sensorless control, and flux-weakening control used for permanent magnet synchronous machines, synchronous reluctance machines, and permanent magnet-assisted synchronous reluctance machines.

Giampaolo Buticchi received the M.Sc. degree in electronic engineering and the Ph.D. degree in information technologies from the University of Parma, Parma, Italy, in 2009 and 2013, respectively.,In 2012, he was a Visiting Researcher with the University of Nottingham, Nottingham, U.K. Between 2014 and 2017, he was a Postdoctoral Researcher with the University of Kiel, Kiel, Germany. He is currently a Professor of Electrical Engineering with the University of Nottingham, Ningbo, China.